# Scalable All-Evaporation Fabrication of Efficient Light-Emitting Diodes with Hybrid 2D–3D Perovskite Nanostructures

*Yu Fu, Qianpeng Zhang, Daquan Zhang, Yunqi Tang, Lei Shu, Yiyi Zhu, and Zhiyong Fan\**

**Quasi-2D (Q2D) lead halide perovskites have emerged as promising materials for light-emitting diodes (LEDs) due to their tunable emission, sloweddown carrier diffusion, and improved stability. However, they are primarily fabricated through solution methods, which hinders its large-scale manufacture and practical applications. Physical-vapor-deposition (PVD) methods have well demonstrated the capability for reproducible, scalable, and layer-by-layer fabrication of high quality organic/inorganic thin films. Herein, for the first time, the full-evaporation fabrication of organic–inorganic hybrid ($(BA)_2Cs_{n-1}Pb_nBr_{3n+1}$) Q2D–3D PeLEDs is demonstrated. The morphology and crystal phase of the perovskite are controlled from 3D to 2D by modulating material composition, annealing temperature, and film thicknesses. The confinement of carriers in 3D layers and the energy funnel effect are discovered and discussed. Importantly, a record high external quantum efficiency (EQE) of 5.3% based on evaporation method is achieved. Moreover, a centimeter-scale PeLED (1.5 cm × 2 cm) is obtained. Furthermore, the $T_{50}$ lifetime of the device with an initial brightness of 100 cd m$^{-2}$ is found to be 90 min with a thin layer PMMA passivation, which is among the longest for all PVD processed PeLEDs. Overall, this work casts a solid stepping stone towards the fabrication of high-performance PeLEDs on a large-scale.**

## 1. Introduction

Metal halide perovskites (PRKs) are regarded as promising candidates for the next generation light-emitting diodes (LEDs), owing to their tunable emission wavelength and high color purity.[1] Substantial works have been done to improve device

Y. Fu, Dr. Q. Zhang, Dr. D. Zhang, L. Shu, Y. Zhu, Prof. Z. Fan
Department of Electronic & Computer Engineering
Hong Kong University of Science and Technology
Clear Water Bay, Kowloon, Hong Kong SAR, China
E-mail: eezfan@ust.hk
Y. Fu, Prof. Z. Fan
HKUST-Shenzhen Research Institute
No. 9 Yuexing First RD, South Area, Hi-tech Park, Nanshan
Shenzhen 518057, China
Y. Tang
School of Energy and Environment
City University of Hong Kong
Kowloon Tong, Hong Kong SAR, China

The ORCID identification number(s) for the author(s) of this article can be found under https://doi.org/10.1002/adfm.202002913.

performance, including the carrier balance, interface passivation,[2] cation doping,[3] light extraction improvement,[4] and nano/ microstructure device structure design.[5] As a result, green and near-infrared PeLEDs with a high EQE (>20%) were achieved via the solution process.[5a,b] However, the unsatisfactory upscalability, and reproducibility are still limiting factors for their future practical implementation.[6] As a comparison, PVD methods, for instance, evaporation, have been widely adopted for scalable fabrication of high-quality thin films in industry.[7] Therefore, it is an urgent need to develop a PVD-based PeLED fabrication process.[8] Although an efficiency beyond 20% has been achieved in PRK solar cells from evaporation method,[9] few works have reported PeLEDs through the all-vacuum process.[10] The best performance PeLED (EQE = 3.26%) reported from the evaporation method is based on a 3D PRK.[11] Though the primary research is focused on 3D PRK, the high electron and hole mobilities and low exciton binding energy of 3D PRK lead to low photoluminescent quantum yield (PLQY) at low excitation regimes[12] and a poor electroluminescence (EL) efficiency of a device. Recently, the newly emerged Q2D PRK is gradually gaining attention.[13] In Q2D PRK, the organic cations act as insulating barriers that confine the charge carriers in two dimensions. Due to the energy funneling effect,[14] Q2D perovskites exhibit a higher exciton binding energy compared with the 3D counterpart. Another exciting feature is that 2D PRKs exhibit better stability against moisture and oxygen, and a suppressed ion migration compared with poor crystallinity 3D thin film.[15]

Despite the successful fabrication of low-dimensional PRK through the solution method, the all-vacuum fabrication of low-dimensional PRKs still remains challenging. First, in a typical solution process, crystallization happens when a solution evaporates. However, in a PVD process, each layer of film is deposited sequentially at first, then in-situ crystal nucleation and growth happens when different adjacent layer contacts with each other. Although the highly uniform thin film can be easily obtained, the crystal growth is hard to control in solid-phase, and the thin films tend to be polycrystalline due to the low chemical forming energy.[16] Second, the vapor pressure of each component may have a huge

**ADVANCED
SCIENCE NEWS**
www.advancedsciencenews.com

**ADVANCED
FUNCTIONAL
MATERIALS**
www.afm-journal.de

difference, especially for long-chain spacers,[10a,17] thus there is a large evaporation rate disparity among different materials.[13c,18] Third, neither crystalline defects nor lattice mismatch can be easily avoided via PVD.[19] Finally, mixed-dimensional PRKs may not merely be formed by controlling the stoichiometric ratio into the Q2D range. The unit cell size and ion diffusion speed should be both considered.[20] To tackle these issues, post-annealing time and temperature, evaporation rate, choice of spacers as well as evaporation sequence should all be well designed.

Herein, for the first time, we demonstrate full evaporation fabrication of PeLEDs devices with quasi-2D-3D hybrid PRK (Q2D-3D PRK) as a light-emitting layer via sequential evaporation method. In this process, a lead bromide ($PbBr_2$) layer, an organic spacer layer n-butylammonium bromide (BABr), and an inorganic layer cesium bromide (CsBr) are sequentially evaporated on a substrate. Mixed-dimensional outer layer quasi-2D PRK-3D $CsPbBr_3$ PRK core–shell structure is obtained after a short time annealing subsequently. By controlling the ratio of BA:Cs, annealing temperature, as well as the film thickness of each layer precisely, molecular structural modulation from 3D to 2D has been achieved. Intriguingly, 2D nanoflake structured PRK with small crystal size can be achieved under a certain condition. The nanoflakes-formed thin film performs lower-dimensional PRK behavior, especially for PLQY increasing. In that case, the maximum luminance of our devices obtained is 8400 cd $m^{-2}$. The highest EQE obtained is 5.3%, and the average EQE of our devices is 4.6%. To our best knowledge, this performance is by far the highest among the reported PeLEDs fabricated with the evaporation method. Moreover, the most extended $T_{50}$ lifetime of our device with PMMA passivation under an initial brightness of 100 cd $m^{-2}$ is found to be 90 min, which is also the longest among all PVD processed PeLEDs

(Refer to Table S4, Supporting Information). In addition, a large-scale device with a size of 1.5 cm × 2 cm is also fabricated, which illustrates the scalability of our strategy.

## 2. Result and Discussion

### 2.1. Formation of PRK via Evaporation Method and Characterizations

**Figure 1** shows the process flow of material evaporation, and the details can be found in the Experimental Section. Briefly, to form a typical PRK layer, a 40 nm $PbBr_2$ film was first evaporated on an indium-doped-tin oxide (ITO) glass evaporated with copper (II) phthalocyanine (CuPc) film and the thickness is controlled to be the same. Then a BABr film and a CsBr film were sequentially evaporated with a total thickness of 80 nm. And six different BABr/(BABr+CsBr) (in short as B/BC) thickness ratios of 0, 0.33, 0.45, 0.5, 0.67, and 1.00 were explored to control material molecular structure. Specifically, when the B/BC ratio is 0.45, and the total film thickness of BABr and CsBr is 80 nm, the thickness of BABr is 0.45 × 80 nm = 36 nm. Thus the CsBr thickness is 44 nm. The thickness calibration procedure of $PbBr_2$, CsBr, and BABr is detailed in Supporting Information. Figure 1 illustrates that if the B/BC ratio is 0 (process I+IV), the resulting molecular structure is 3D, which has been previously reported.[10b] When the B/BC ratio is 1 (process I+V), the 2D structure is obtained, which has also been reported by the solution process previously.[21] However, when 0<B/BC<1 (process I+II+III), the unique hybrid Q2D–3D structures can be acquired, which has not been reported with evaporation approaches so far to our best knowledge.
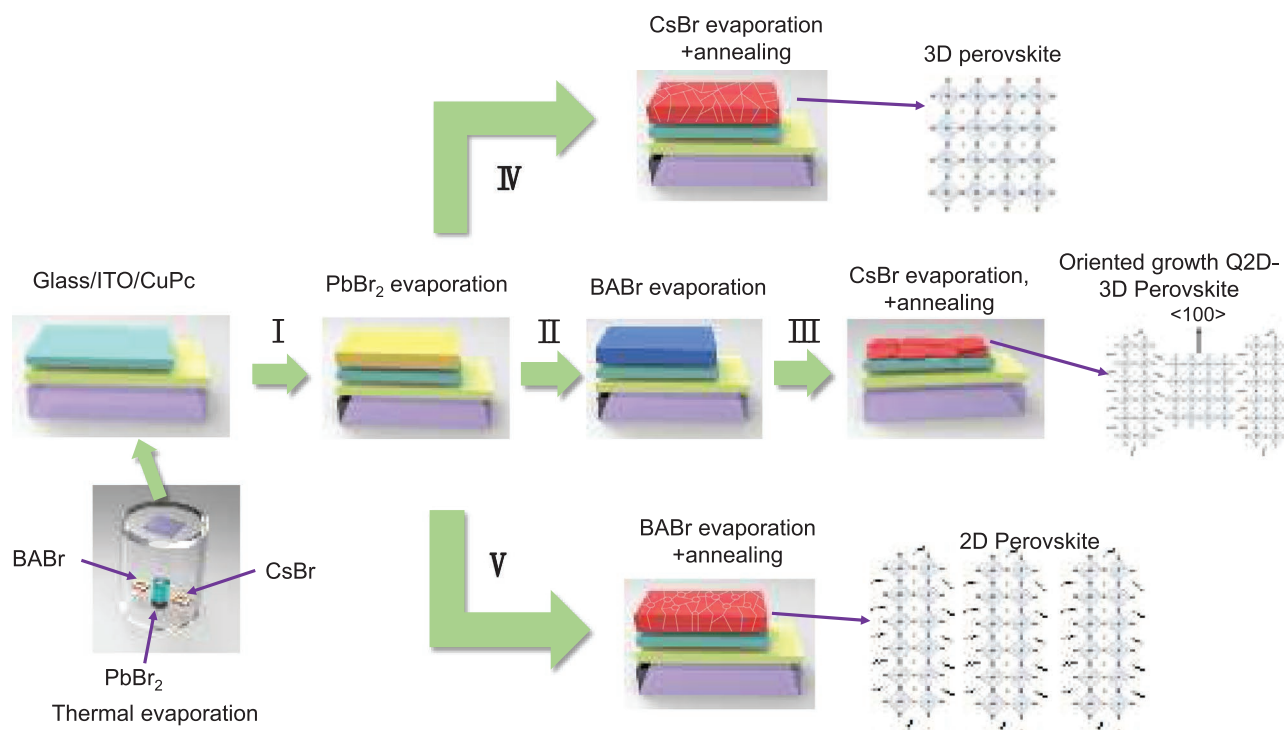


**Figure 1.** Process flow to fabricate 3D PRK (I+IV), 2D PRK (I+V), and Q2D-3D PRK (I+II+III) via PVD.
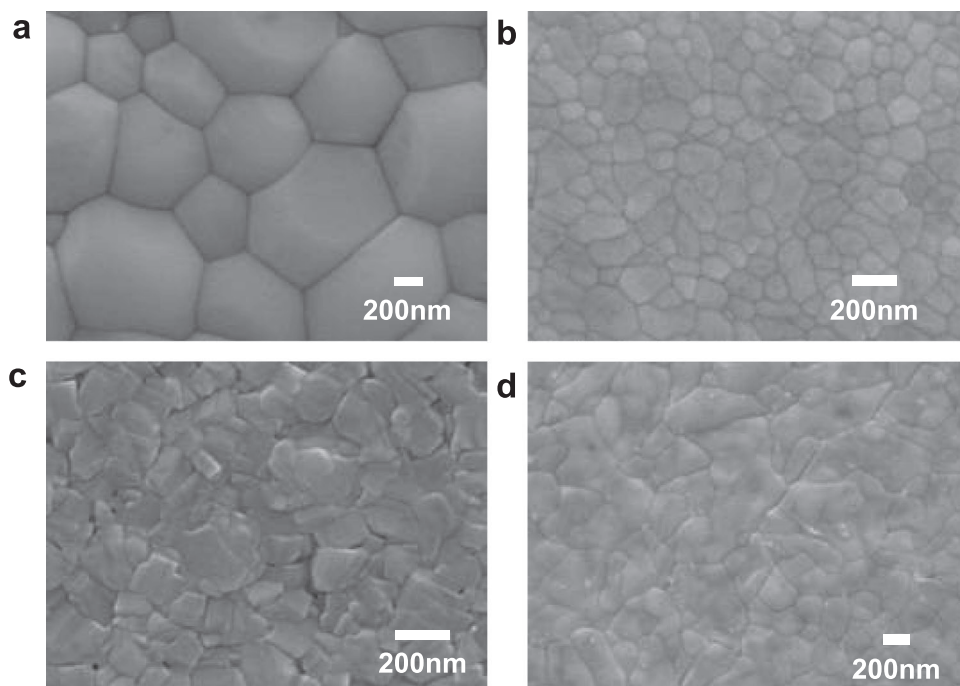
**Figure 2.** SEM images of PRK films: a) CsPbBr$_3$ 3D PRK after 260 °C 10 min postannealing. b) Q2D-3D PRK film with 0.33-B/BC after 160 °C 5 min postannealing. c) Q2D-3D PRK film with 0.45-B/BC after 160 °C 5 min postannealing. d) Q2D-3D PRK film with 0.67-B/BC after 160 °C 5 min postannealing.

The morphology of the PRK films deposited on glass/ITO/CuPC is studied by scanning electron microscopy (SEM), as shown in **Figure 2**. Figure 2a shows the 3D PRK film after 260 °C postannealing for 10 min exhibiting good morphology with a compact layer of large grain-size crystals (≈1 μm). As a comparison, the crystal size decreases apparently as the B/BC ratio increases. Compared with 3D PRK, the annealing temperature of BA cation induced Q2D–3D PRK is lowered down to 160 °C. To control the influence of temperature, all the following control groups are postannealed at 160 °C for 5 min. For 0.33-B/BC PRK film (Figure 2b), the grain size shrinks to 300 nm and finally forms a compact layer. When the B/BC ratio reaches 0.45 (Figure 2c), the compact and uniform film shows 2D nanoflakes structure with multiple interlayers in each crystal grains. Note that we have also found that if 0.45-B/BC PRK film without annealing is placed in air for an hour, the as-deposited film becomes loosely packed with pinholes (Figure S1, Supporting Information). Typically, an annealed thin film has a grain size of 100 to 200 nm with a multilayer structure (Figure 2c), implying that the BA plays an important role as a spacer to confine the growth of crystals. The improved morphology can be attributed to the ordered growth with higher crystallinity during the annealing process. Even though the size of the crystal is not reduced obviously when the B/BC ratio reaches 0.67 (Figure 2d), the nanoflake structure disappears under 160 °C postannealing, and grain boundaries are not obvious at all. However, when the postannealing temperature decreases to 140 °C, the nanoflake structure appears with a smeared boundary (Figure S4c,d, Supporting Information). It can be attributed to the hindered nucleation by the long-chain group. The influence of annealing temperature and time will be discussed systematically later. Interestingly, the pure BA$_2$PbBr$_4$ film after annealing shows a

morphology with the maximum attainable crystal grains around 4 μm surrounded by a number of small grains (Figure S5a,b, Supporting Information). The crystal grains are compact and appear like 3D CsPbBr$_3$ PRK with diverse crystal sizes. This result confirms that the crystallinity of BA$_2$PbBr$_4$ is poor and unit cell size ($a = 8.322(8)$Å, $b = 8.184(9)$ Å, $c = 27.66(3)$ Å, and $\alpha = \beta = \gamma = 90°$ in orthorhombic phase) is far larger than CsPbBr$_3$ unit cell ($a = b = c = 5.95$ Å, and $\alpha = \beta = \gamma = 90°$ in cubic phase) though the BA$_2$PbBr$_4$ is easy to form due to low chemical forming energy.[22] To further verify the uniformity of our evaporated PRK thin film, low magnification SEM for both a top-view and a cross-sectional view of 0.45-B/BC thin film after postannealing are provided in Figure S3a,b, Supporting Information. Both images reveal that our thin film is highly uniform and smooth macroscopically.

To further understand the formation mechanism of Q2D-3D PRK nanoflakes, the influence of annealing temperature and time on the crystallinity is also investigated. Generally, both lower postannealing temperature and shorter annealing time induce a Q2D-structural PRK due to the restricted growth of BA cation (Figures S4c,d, S5, and S6, Supporting Information). While with proper B/BC ratio (such as 0.5, Figure S4e,f, Supporting Information), the reaction happens at room temperature because of fast thermodynamics. When PbBr$_2$ and BABr are sequentially deposited, the octahedral structured PbBr$_6$ monolayer sheets generate at first, then BA cation will take over corner-sharing sites of lead halide 3D framework, while the BA with a large ionic radius will separate PbBr$_6$ into a layered structure. In that case, vertically aligned plate-like 2D-phase crystallites will generate at the interface between the PbBr$_2$ layer and the BABr layer. After the CsBr layer is deposited, both Cs$^+$ and Br$^-$ ions diffuse through a foresaid 2D layer barrier structure then are confined inside, and finally form Q2D-confined PRK nanoflakes, as we
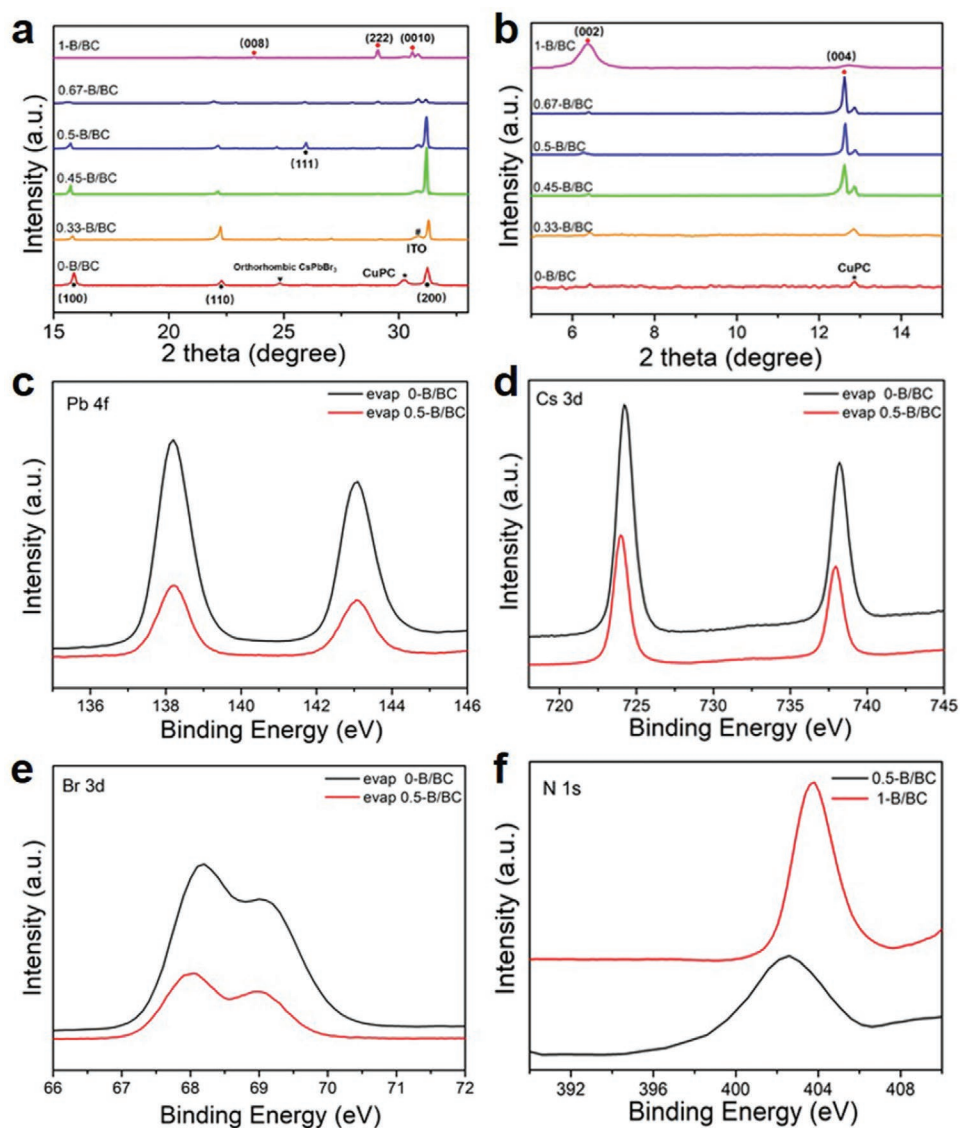
**Figure 3.** a) XRD diffraction pattern of 3D PRK, 2D PRK and Q2D-3D PRK $BA_2Cs_{n-1}Pb_nBr_{3n+1}$ film with different proportion of B/BC. b) XRD pattern of 3D PRK, 2D PRK, and Q2D-3D PRK $BA_2Cs_{n-1}Pb_nBr_{3n+1}$ film with different proportion of B/BC at small angles. All the peaks marked by black dots represent 3D phase PRK, and peaks marked by red diamonds represent 2D phase PRK. XPS spectra of the high-resolution c) Pb 4f core-levels, d) Cs 3d core-levels, e) Br 3d core-levels between 3D PRK (0-B/BC) and Q2D-3D PRK (0.5-B/BC) and f) N 1s core-levels between 0.5-B/BC and 2D PRK (1-B/BC).

observed. With short annealing time and low annealing temperature, the barrier layer can stay stably so that the $Cs^+$ and $Br^-$ diffusion can be facilitated, which eventually leads to the formation of the Q2D–3D structure. In contrast, the confinement of barrier structure can be weakened either under high annealing temperature or after excessively long annealing time, which will be discussed later. In this case, the thin film shows a tendency to form the larger crystal grains, which is similar to 3D PRK. The schematic diagram of the mechanism is shown in Figure S8 (Supporting Information). Moreover, to verify the effect of the barrier structure formed at the $BABr/PbBr_2$ interface, the reversed evaporation sequence followed by $PbBr_2$-CsBr-BABr was also implemented (Figure S9, Supporting Information). The component proportion is the same as the previous 0.5-B/BC PRK film after 160 °C and 5 min postannealing.

In contrast, an excessive amount of unreacted Cs/BA halides at the top reflects inferior uniformity and morphology of as-prepared thin film without showing nanoflake-like grains. The X-ray diffraction (XRD) pattern of the reversed evaporation sequence $PbBr2$-CsBr-BABr sample is provided in Figure S10 (Supporting Information). The XRD pattern illustrates that the reversed sequence thin film is a mixed phase of $CsPbBr_3$, $CsPb_2Br_5$, $Cs_4PbBr_6$, unreacted CsBr, and orthorhombic $CsPbBr_3$. This result reveals that large BA cations cannot penetrate through $CsPbBr_3$ with smaller unit cell size so that it is difficult to form mixed-dimensional PRK.

The effect of varying B/BC ratios on the crystal structure of PRK films on CuPc/ITO substrates is studied using XRD (**Figure 3**a). The peaks at 30.2° and 30.7° can be attributed to the lattice plane of CuPc and ITO substrate, respectively. For

ADVANCED
SCIENCE NEWS

www.advancedsciencenews.com

ADVANCED
FUNCTIONAL
MATERIALS

www.afm-journal.de

3D PRK (0-B/BC), we assign all crystal facets reflections ((100), (110), (111), and (200)), to the cubical 3D PRK polycrystalline phase. With the BA introduced, peak intensities of ($h$00) ($h$ = 1, 2) diffractions increase significantly as the B/BC ratio increases from 0 to 0.45, revealing a preferential growth of 3D phase PRK along [100] zone axis. When the B/BC ratio increases further, the intensities of 3D ($h$00) facets diffraction decreases. A series of new diffractions marked as (00l) emerge, corresponding to characteristic peaks of 2D phase PRK. In that case, the phase transition from 3D PRK to 2D PRK happens gradually when we increase BA concentration.[23] Besides, diffraction peak positions of (100), (110), and (200) belonging to 3D phase PRK all show a negative shift in the case of the substitution of Cs by BA with a larger ionic radius. We use Bragg's law to calculate the lattice constant increase from 5.63 Å to 5.88 Å when the B/BC ratio increases from 0 to 0.67 (see details in Supporting Information), which indicates the formation of Q2D–3D PRK heterostructure. To further prove the existence of the 2D phase PRK and the phase transition, a small-angle XRD result is discussed (Figure 3b). Peak locates at 12.9° associated with CuPc can be dismissed. As B/BC ratio increases, the intensities of two peaks located at 6.3° and 12.6° can be detected, which are diffraction peaks of multiple $n$ ($n$ represents the layer number of $PbX_6$ sheets) in 2D phase PRK. In addition, for Q2D-3D PRK with B/BC ratio between 0.45 and 0.67, the intensity of (004) facet peak is far stronger than that of (002) one, suggesting that (004) facet is more preferred when forming Q2D–3D hybrid PRK. BA cations promote the formation of 2D perovskite and facilitate preferential growth of inorganic PRK multi-layers. Specifically, pure 2D phase $BA_2PbBr_4$ thin film prepared by the evaporation process is demonstrated as well.[24] The peak intensity of (002) is much higher than (004) facet, which means a single layer 2D phase PRK is more preferred. Furthermore, the full width at half maximum of both peaks are broadened, which illustrates the size decrease of crystallite. XRD on 0.45-B/BC PRK film without post-annealing after being placed in air for an hour and after a long time (1 and 2 h) postannealing at 160 °C are both carried out to study the phase transition influenced by annealing (Figure S2a,b, Supporting Information). The unannealed film shows a mixed phase of cubic and orthorhombic due to low crystallization temperature. After a long time postannealing at 160 °C, only cubic phase PRK forms, and the preferential growth along [100] zone axis is inhibited as (110) and (111) diffraction peak intensity increases. Besides, XRD results for 1 and 2 h do not show the obvious difference, revealing ion migration is completed after 1h annealing. This phase transition process is also accompanied by film color change, as shown in Figure S7 (Supporting Information). Namely, the as-prepared film has high transparency in the beginning. After an hour, the film color turns into yellow gradually. Moreover, the film with post-annealing appears more yellowish.

X-ray photoelectron spectroscopy (XPS) measurement is carried out to characterize the atomic ratios, the binding energy of each element, and the electronic structure of our PRK films. The high-resolution XPS spectra are performed to indicate the bonding situation of Pb, Cs, and Br (Figure 3c-e). Based on the Pb 4f core-level spectrum in Figure 3c, chiefly, there is no signal of metallic Pb existence for both 3D and Q2D-3D VD processed PRK thin film, indicating all Pb has fully reacted into

PRK. Meanwhile, 3D $CsPbBr_3$ (0-B/BC) PRK films after post-annealing show two peaks located at 138.2 and 143.1 eV, manifesting the formation of Pb–Br bonding whereas both peak positions have a 0.1 eV negative shift in 0.5-B/BC thin film. Similarly, the Q2D-3D PRK binding energy peaks of both Cs (Figure 3d) and Br (Figure 3e) elements also tend to shift toward lower binding energy (by 0.46 and 0.2 eV, respectively) compared with 3D PRK. This result is on account of a change in the chemical bonding. On the other hand, we analyzed N 1s spectrum (Figure 3f) between 0.5-B/BC and 1-B/BC where N element only exists in BA cations. Compared with 2D PRK (1-B/BC), N 1s peak position of Q2D-3D PRK (0.5-B/BC) shows a 1.7 eV negative shift. It means when the BA groups are binding with core Pb by replacing Cs, the electrons exist in N will move toward center metal atom, resulting in the binding energy increase of N element. During the phase transition from 3D to 2D, the ammonium salt in long chain group can replace the Cs and passivate the Br, which reduces the binding energy of Cs and Br. As a comparison, Pb, namely the center of a unit cell, has no direct contact with the ammonium salt. Therefore, the binding energy of Pb is less affected. The film uniformity and element distribution are also further confirmed by scanning electron microscopy (SEM) images (Figure S11a–d, Supporting Information). The valance band (VB) edge potential of the thin films with different BA ratios are measured by the XPS valance band spectrum as well (Figure S12, Supporting Information). The VB energy levels of 0-B/BC, 0.33-B/BC, 0.45-B/BC, 0.5-B/BC, and 0.67-B/BC after calculation as −5.97, −5.98, −5.98, −6.1, and −6 eV, respectively. Besides, the atomic ratios of different BA ratio materials are characterized by both XPS (Table S1, Supporting Information) and EDX (Figure S11e, Supporting Information).

The steady-state UV–visible (UV–vis) absorption spectra of PRK thin films with different B/BC ratio are shown in **Figure 4**a. The former five PRK films show continuous absorption bands with onsets corresponding to an optical bandgap, which is estimated from the Tauc plot (Figure S13, Supporting Information), shifting from 2.25 to 2.34 eV, respectively. It fits well with the corresponding steady-state photoluminescence (PL) peaks (Figure 4b). While for the 2D PRK film, a steep absorption band edge can be observed at 335 nm, implying that the spacer induced PRK laminates to possess large bandgap to be an excellent quantum well material. In addition, two absorption peaks at ≈434 and ≈463 nm for 0.5 and 0.67-B/BC samples are quasi-2D exciton absorption peaks. This result is consistent with the following transient absorption (TA) measurement. The steady-state PL spectra of PRK films with different B/BC ratios are shown in Figure 4b. The peak position at 551 nm was observed for the pure 3D PRK. Then the peak position is blue-shifted gradually to 529 nm when the ratio of B/BC is increased to 0.67, which indicates the proportion of small $n$ increased. The shoulder peaks appeared in 0-B/BC, and 0.67-B/BC are attributed to the noise of PL background as a result of low PLQY of these two samples (0.6% and 0.2%, respectively). The PLQY of 0.45-B/BC PRK thin film is 26.9%, which is the highest among all different B/BC ratios PRK film. Both the PL peak blueshift and PL enhancement can be ascribed to the formation of the quantum well structure. TA experiments are utilized to investigate both the photoexcitation process and energy transfer
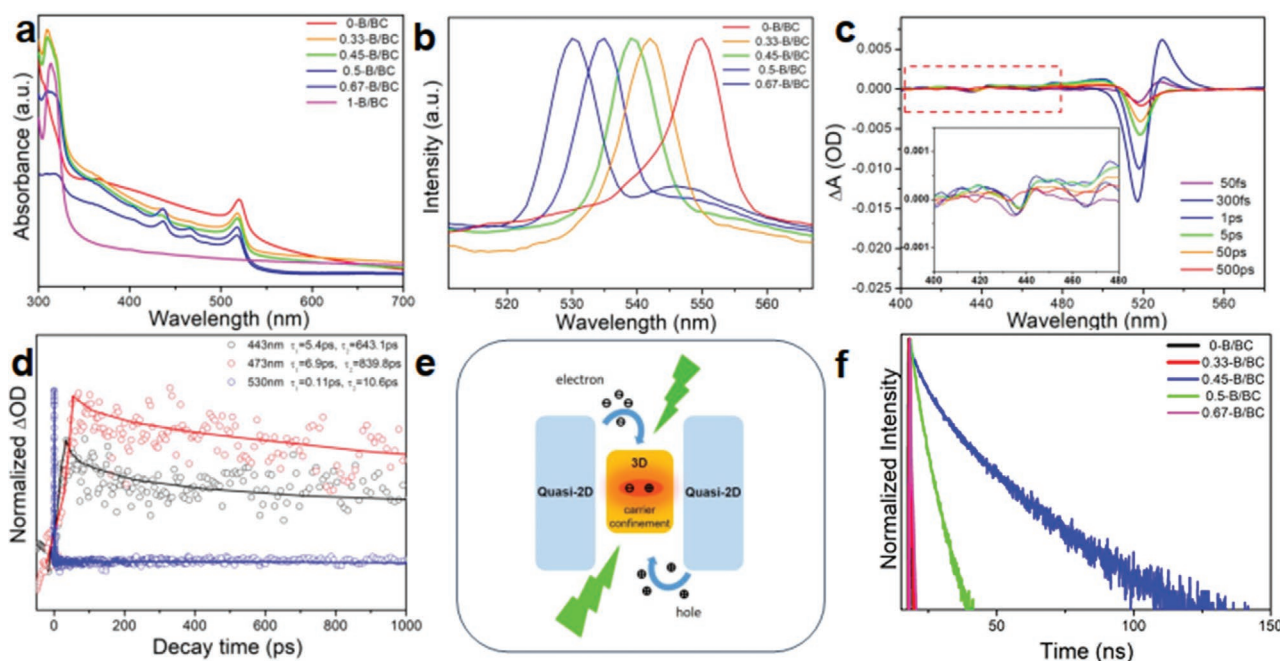
**Figure 4.** a) Steady-state UV–vis (UV–vis) absorption spectra. b) Steady-state PL spectra. c) Transient absorption (TA) spectra of 0.45-B/BC ratio Q2D-3D PRK film under different decay times. d) TA kinetics at 300 fs with multiple ESA peaks at 443, 473, and 530 nm, respectively. e) Schematic illustration of the carrier confinement effect that happened inside Q2D-3D PRK nanoflake. f) Time-resolved photoluminescence (TRPL) spectra of typical PRK films.

dynamics in the Q2D-confined PRK film. Figure 4c shows the decay time-resolved TA properties with the best EL performance (0.45-B/BC). The strongest ground state bleach (GSB) peak locates at about 518 nm and the accompanying excited state absorption (ESA) peak at around 530 nm can be regarded as characteristic peaks of excitonic absorption of 3D PRK.[11,21b] Whereas several GSB peaks related to different $n$-value species ($n = 2$ at ≈432 nm, $n = 3$ at ≈463 nm) in quasi-2D PRK packed together and they are hard to be distinguished. The weak signals of quasi-2D PRK owe to both small proportion of quasi-2D components and strong GSB and ESA signal of 3D ($n > 5$) PRK. All peak positions are in good agreement with UV–vis absorption measurement. Besides, GSB peak associated with larger bandgap composition of quasi-2D layer come out before 50 fs, then two red-shifted signals at ≈463 nm and 530 nm ascend rapidly within 300 fs then decay afterward. This process reveals that carriers are first formed in the outer larger bandgap layers, then travel into the smaller bandgap components. The decay kinetics at 300 fs with multiple ESA peaks are further investigated in Figure 4d. The fast decay time constants at 530 nm (0.11 ps) are considered as the cooling of above-bandgap photogenerated charges. The intermediate decay time displays an increasing trend from 5.4 ps at 443 nm to 6.9 ps at 473 nm and then to 10.6 ps at 530 nm, ascribing to the energy transfer route from large bandgap barrier components to small bandgap light-emitting domain component, which is consistent with the funneling effect from time-resolved TA result. While the slow decay time constants are assigned to nonradiative charge trapping. Compared with high energy components, the lower energy inlayer component shows no trap states decay time via binary fitting, which

indicates that the concentration of carriers increases because of the funnel effect under excited states facilitating efficient radiative recombination. The schematic of carrier funneling into 3D PRK, facilitating efficient radiative recombination, is shown in Figure 4e. To study the electron–hole pairs recombination kinetics, time-resolved photoluminescence (TRPL) measurement was carried out (Figure 4f). The kinetics decay curves are fitted in two amplitudes, where a short lifetime is associated with trap state induced nonradiative recombination, and a long lifetime belongs to radiative recombination within PRK grains. As B/BC ratio increases from 0 to 0.5, lifetimes for both of two amplitudes and the averaged value rises (from $\tau_1 = 0.6214$ ns, $\tau_2 = 2.9$ ns, $\tau_{average} = 0.789$ ns to $\tau_1 = 7.691$ ns, $\tau_2 = 25.222$ ns, $\tau_{average} = 13.606$ ns). Meanwhile, the weight of long lifetime also increases as higher B/BC ratio is introduced. It means that the density of trap states reduces when the BA ratio increases, which meanwhile increases the radiative recombination rate. However, PL lifetime decays rapidly when the B/BC ratio increases to 0.67. We hypothesize that the deteriorated lifetime can be attributed to poor film crystallinity and more defects induced by high tolerance of BA group in the crystal cell (Table S2, Supporting Information).

To realize all-evaporation processed PeLEDs, a number of factors should be taken into consideration, such as band energy alignment between PRK layer and charge injection layers, thermal evaporation processability, and high-temperature tolerance of all materials as well as film uniformity. In the quest for a proper hole injection material, it was found that CuPc has several distinct advantages such as being evaporable, possessing high hole mobility, and decent stability. Therefore, CuPc has been widely used in organic photovoltaics and OLEDs. Herein,
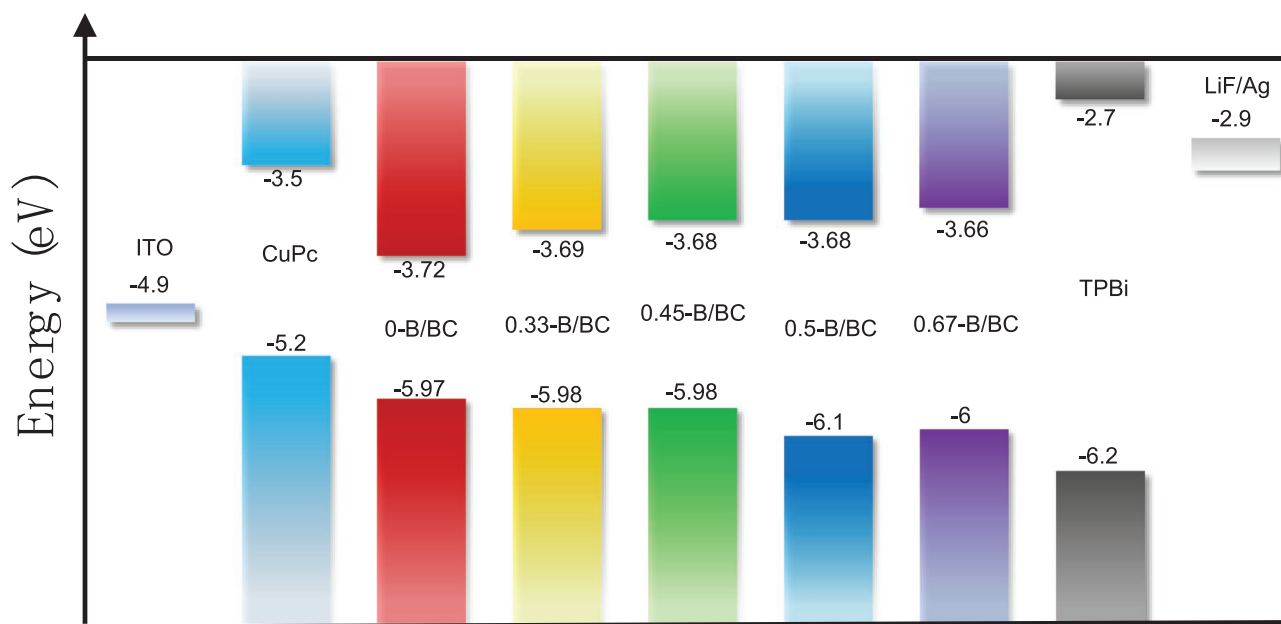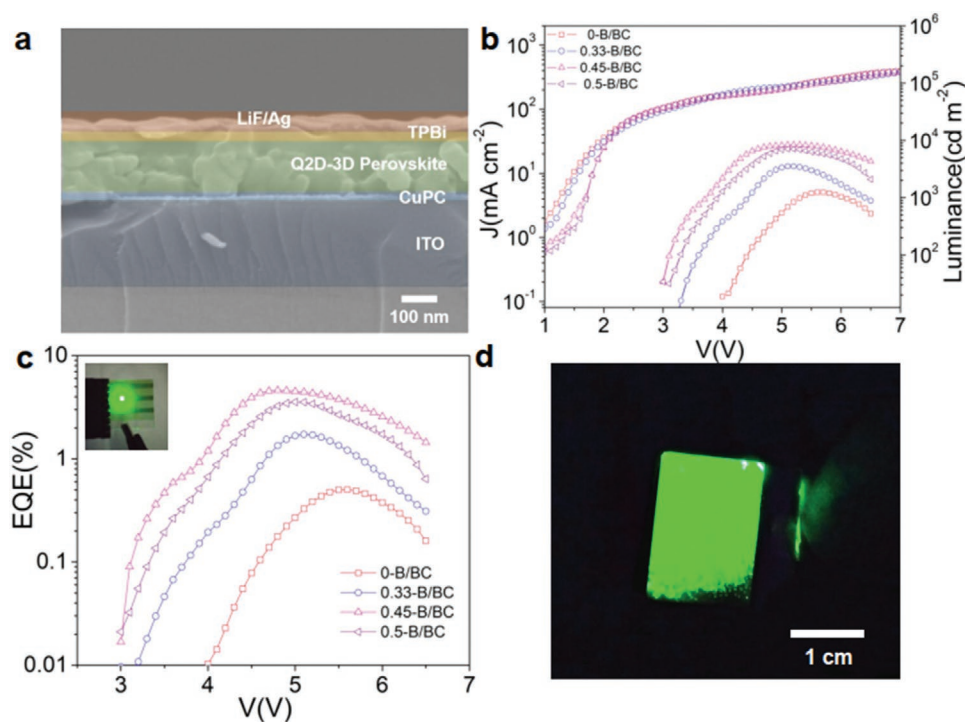
**Figure 5.** Band energy diagram of LEDs fabricated via typical PRK films with various B/BC ratios.

we evaporated CuPc (20 nm) as a hole-injecting, and electron-blocking interlayer, 1,3,5-tris(1-phenyl-1H-benzimidazol-2-yl) benzene (TPBi) (50 nm) was used as electron-transporting and hole blocking layer on the top of the emission layer owing to its proper band alignment with the active layer. The band structure of Q2D–3D PRK at 0.5-B/BC ratio was obtained by the measurement of both XPS and Tauc plot. The band alignment diagram after calculation among all different BA proportions that we induced in EL devices is shown in **Figure 5**. Both valance band ($E_v$) and conduction band ($E_c$) among varied B/BC ratios PRK active layer fit well with charge injection layers on both sides.

## 2.2. Light-Emitting Diodes

PeLEDs based on different BA ratio Q2D–3D PRK and 3D PRK films have been fabricated, followed by the device structure mentioned above. The cross-sectional SEM image (**Figure 6**a) shows a typical device architecture. The layers from the bottom to top correspond to ITO (280 nm), CuPc (≈20 nm), 2D PRK (≈200 nm), TPBi (≈50 nm), and LiF (3 nm)/Ag (100 nm), respectively. The current density–voltage–luminance (J–V–L) curves of different devices were tested and exhibited in Figure 6b. Compared with 3D PRK (0-B/BC) device, the J of Q2D-3D PRK (0.33-B/BC, 0.45-B/BC, 0.5-B/BC, and 0.67-B/BC) at low voltage range (0–1 V) decrease as B/BC ratio rises. The long-chain BA groups can effectively suppress the current leakage. At the operating voltage (3-6 V), the current density of 0.67-B/BC device is still lower than the rest of device before 4.5 V. However, it starts to soar beyond 4.5 V and finally reached 452 mA cm$^{-2}$ at 5.5 V, which is much larger than that of other devices (Figure S20, Supporting Information). This result implies that the high ratio of BA cations can slow down the carrier diffusion when the weak electric field is induced. While at high voltage bias, more

defects will be created between crystal boundaries of adjacent 2D PRK nanoflakes as the temperature of the device increased. Besides, the inferior crystallinity of 0.67-B/BC PRK verified by both XRD and SEM also reveals that more trap-state induced nonradiative recombination happens at a higher voltage. With the augment of B/BC proportion from 0 to 0.5, the EL emission intensity of the device is also increased. Whereas the luminance of the 0.67-B/BC device is too low (<10 cd m$^{-2}$) to be detected, so that the EL property and EQE will not be further discussed. The turn-on voltages based on Q2D–3D PRK devices with 0.33, 0.45, and 0.5 B/BC are at 3.2, 2.9, and 2.8 V, respectively. All of them are lower than that of 3D PRK (4.1 V). This result reveals that the charge injections are more balanced and efficient in Q2D–3D PRK. Compared with the maximum luminance of 0-B/BC (1300 cd m$^{-2}$), 0.33-B/BC BA (3700 cd m$^{-2}$) and 0.5-B/BC BA (7400 cd m$^{-2}$), the maximum brightness occurs on the 0.45-B/BC device with around 8400 cd m$^{-2}$ at 4.7 V. The EL spectrum (Figure S14, Supporting Information) shows the peak position is blue-shifted along with peak broadening as the B/BC ratio increases, which is consistent with PL result. Figure 6c displays the EQE versus voltage plot among the PeLEDs with four different B/BC ratios. The typical peak EQE is achieved as 4.6% for the 0.45-B/BC based Q2D–3D PRK device under 4.5 V bias. Moreover, the highest peak EQE obtained is 5.3% (Figure S17, Supporting Information). To our best knowledge, this EQE is by far the highest among green light PeLEDs fabricated via the PVD method, as summarized in Table S4 (Supporting Information). The maximum EQE of the rest devices are 3.8% (0.5-B/BC) at 5 V, 1.85% (0.33-B/BC) at 5 V and 0.54% (0-B/BC) at 5.5 V, respectively. These results also illustrate that the Q2D–3D PRK devices possess smaller turn-on voltage and leakage current due to confinement of carriers inside quasi-2D PRK. To further balance charge injection and improve device performance, a thin layer of PMMA is spin-coated onto the PRK layer before TPBi deposition (Figure S15, Supporting

**ADVANCED
SCIENCE NEWS**
www.advancedsciencenews.com

**ADVANCED
FUNCTIONAL
MATERIALS**
www.afm-journal.de

**Figure 6.** a) Cross-sectional SEM image of the Q2D-3D PRK device architecture. b) Current density– voltage– luminance (*J–V–L*) curves of devices in different B/BC ratios. c) EQE curves of devices in different B/BC ratios. Inset figure shows optical photo for 0.45-B/BC device driving at 4.5 V. d) Optical photograph of scalable device demonstration with optimized condition with 1.5 × 2 cm² effective luminous area with a bias of 5 V. Inset figure shows device area under environment light.

Information). After inserting in PMMA layer, the current density under bias decreases due to improved carrier balance, while the maximum luminance drops to 7600 cd m⁻². In that case, the device EQE is further improved to 5.56% due to higher current efficiency. Besides, the device performance based on 0.45-B/BC ratio with different light emitting material (LEM) thicknesses (120 and 600 nm) is demonstrated as well, which is much worse than that of 200 nm thick LEM device shown previously (Figures S16 and S17, Supporting Information). The poor performance of the thinner LEM layer device is mainly caused by current leakage and defects triggered by inferior uniformity and morphology. In contrast, the inferior performance of the thicker LEM layer can be attributed to the incomplete crystallization and incomplete reaction. To inspect the lifetime ($T_{50}$) of our devices, time-dependent EL measurement with an initial brightness of 100 cd m⁻² in the ambient environment (23 °C, 60% relative humidity) is demonstrated (Figure S18, Supporting Information). The lifetime of the device with and without a thin layer of PMMA under optimized fabrication conditions are both measured after being encapsulated with epoxy. After inserting the inlayer PMMA and encapsulating the cathode side of the device with epoxy, the device displayed a longer lifetime (90 min) than a device with no PMMA (62 min), which shows a reasonably longer lifetime compared with results on evaporation method fabricated PRK layer PeLEDs reported in Table S4 (Supporting Information). To further prove the advantage of PMMA in physically blocking water and oxygen in air, SEM images of PRK films covered with/without PMMA after 7 d placement in the ambient environment (average temperature

around 25 °C, with 60% moisture) are shown in Figure S19 (Supporting Information). The PRK film with PMMA passivation has better film quality with much less pin-hole than the film without PMMA, revealing the improved stability. To verify the reproducibility of our Q2D–3D PRK based on the sequential vacuum deposition technique, 24 devices from four different batches were fabricated under the same optimized fabrication condition (0.45-B/BC) and the identical measurement condition. We obtained an EQE distribution histogram in Figure S21 (Supporting Information). It can be seen that the weighted arithmetic mean EQE value was 4.6%, which is marginally lower than our highest EQE 5.3%. The promising results demonstrated the great potential of this fabrication method in future scalable production of PeLEDs with further improvement in performance and life-time. In order to demonstrate the upscaling capability, a large area LED (1.5 cm × 2 cm) based on an optimized recipe is demonstrated. When the device area scales up, a higher driving voltage is needed due to the undesired parasitic resistance. Therefore, more severe Joule heating will happen due to a higher driving voltage. Besides, charge recombination occurs at interface, and even inside charge injection layer, under high driving voltage due to imbalanced carrier mobilities in each layer. When we increase the thickness of CuPc layer to 30 nm, the large area EL device turned on partially at 4.5 V. After increasing driven voltage to 5 V, the luminance has good uniformity, and the lighting area enlarges to almost the whole device area (Figure 6d). The current density increases compared with our standard small size device, with EQE equal to 0.54% based on *J–V–L* and EQE curves in

**ADVANCED
SCIENCE NEWS**
www.advancedsciencenews.com

**ADVANCED
FUNCTIONAL
MATERIALS**
www.afm-journal.de

Figure S15 (Supporting Information). This low EQE can be explained by the parasitic resistance from the electrodes, as well as the particulate contamination from the environment since our fabrication process is not performed in a cleanroom.

## 3. Conclusion

In summary, here we demonstrate organic–inorganic hybrid $((BA)_2Cs_{n-1}Pb_nBr_{3n+1})$ Q2D–3D PRK LEDs fabrication via an all-evaporation process for the first time. Systematic characterizations, including XRD, SEM, and ultrafast spectroscopy technique combined with optical measurement, were utilized to confirm the embedded structure of this Q2D–3D PRK material. The morphology of the PRK films was controlled by tuning the thickness ratio of BABr/(BABr+CsBr), annealing time, and temperature. It was discovered that the proper amount of BA can not only improve the crystallinity in preferential orientation growth but also play a vital role as a barrier to slow down the carrier injections for more efficient radiative recombination. PeLEDs have been fabricated based on this nanocomposite material, and the effect of different proportions of BA has been systematically studied. Intriguingly, the devices have demonstrated the maximum luminance of 8400 cd m$^{-2}$ and the highest EQE of 5.3%, respectively, which is the highest for PeLEDs made by evaporation method to our best knowledge. It is also found that the introduction of both inorganic Cs cations and Q2D–3D- PRK leads to better device stability than conventional organic MA/FA 2D or quasi-2D PRK LEDs. Moreover, a large scale device with a size of 1.5 cm × 2 cm is also demonstrated. Overall, the work performed here paves a promising route towards the scalable fabrication of high-performance PeLEDs for broad applications such as lighting and displays in the future.

## 4. Experimental Section

*Materials*: ITO-coated glass substrates were purchased from NOZO Technology Co., Ltd. The CsBr, PbBr$_2$, BABr, CuPc, TPBi were all purchased from Sigma-Aldrich. All materials were used as received.

*Device Fabrication*: The substrates were sequentially washed in ultrasonic cleanser with Triton X-100 water solution, isopropanol, acetone, ethanol, and deionized water. The sheet resistance of ITO is 6–8 Ω sq$^{-1}$, and the thicknesses of glass and ITO are 1.1 mm and 300 nm, respectively. The average transmittance of ITO glass in the visible region is 82%.

*Preparation of PRK Film and Device Fabrication*: The thickness of each deposited layer through thermal evaporation process is controlled by a thickness monitor. 20- 30 nm thick CuPc as hole injection material was deposited on ITO glass by evaporation with a deposition rate from 1.5 to 2.3 Å s$^{-1}$. After CuPc deposition, a post-annealing process (150 °C, 10 min) is induced. The CuPc coated ITO substrates were transferred to a vacuum chamber and evacuated to a pressure of $4 \times 10^{-4}$ Pa for the following PbBr$_2$, BABr, and CsBr sequential vapor deposition. The sources were located at the bottom of the chamber with an angle of 90° with respect to the substrates while 45° to each other. The distance between the source and substrate was 20 cm. Lead bromide and other organic–inorganic bromides of different ratios were placed in two separate crucibles for sequential vapor deposition. Typically, Lead bromide (40 nm, 1.5-1.7 Å s$^{-1}$), BABr (35 nm, 3.8–4 Å s$^{-1}$) and cesium bromide (45 nm, 2.8–3.1 Å s$^{-1}$) were evaporated sequentially to generate

as-cast organic–inorganic hybrid PRK films. The as-deposited PRK films were postannealed at 160 °C for 0, 5, 10, and 20 min on a hotplate. To further improve the charge injection balance, a thin layer of PMMA was prepared after PRK film deposition. In detail, 100 µL of PMMA solution (0.5 mg mL$^{-1}$ in acetone) was spin-coated onto PRK film at 5000 r.p.m. for 60 s in the glovebox. To complete the device, TPBi (50 nm, 1.5–2.3 Å s$^{-1}$), LiF (1.5 nm, 0.9 Å s$^{-1}$), and Ag (3.5–5 Å s$^{-1}$) were deposited on the PRK film sequentially by thermal evaporation.

## Supporting Information

Supporting Information is available from the Wiley Online Library or from the author.

## Conflict of Interest

The authors declare no conflict of interest.

[1] a) Z. Xiao, R. A. Kerner, L. Zhao, N. L. Tran, K. M. Lee, T.-W. Koh, G. D. Scholes, B. P. Rand, *Nat. Photonics* **2017**, *11*, 108; b) Z.-K. Tan, R. S. Moghaddam, M. L. Lai, P. Docampo, R. Higler, F. Deschler, M. Price, A. Sadhanala, L. M. Pazos, D. Credgington, *Nat. Nanotechnol.* **2014**, *9*, 687.

[2] a) J. Wang, N. Wang, Y. Jin, J. Si, Z. K. Tan, H. Du, L. Cheng, X. Dai, S. Bai, H. He, *Adv. Mater.* **2015**, *27*, 2311; b) X. Yang, X. Zhang, J. Deng, Z. Chu, Q. Jiang, J. Meng, P. Wang, L. Zhang, Z. Yin, J. You, *Nat. Commun.* **2018**, *9*, 570.

[3] a) L. Zhang, X. Yang, Q. Jiang, P. Wang, Z. Yin, X. Zhang, H. Tan, Y. M. Yang, M. Wei, B. R. Sutherland, *Nat. Commun.* **2017**, *8*, 15640; b) X. Zhang, H. Liu, W. Wang, J. Zhang, B. Xu, K. L. Karen, Y. Zheng, S. Liu, S. Chen, K. Wang, *Adv. Mater.* **2017**, *29*, 1606405; c) L. N. Gil-Escrig, A. Miquel-Sempere, M. Sessolo, H. J. Bolink, *J. Phys. Chem. Lett.* **2015**, *6*, 3743; d) C. Wu, T. Wu, Y. Yang, J. A. McLeod, Y. Wang, Y. Zou, T. Zhai, J. Li, M. Ban, T. Song, *ACS Nano* **2019**, *13*, 1645.

[4] a) Q. Zhang, M. M. Tavakoli, L. Gu, D. Zhang, L. Tang, Y. Gao, J. Guo, Y. Lin, S.-F. Leung, S. Poddar, *Nat. Commun.* **2019**, *10*, 727; b) S. Jeon, L. Zhao, Y. J. Jung, J. W. Kim, S. Y. Kim, H. Kang,

J. H. Jeong, B. P. Rand, J. H. Lee, *Small* **2019**, *15*, 1900135; c) L. Zhao, K. M. Lee, K. Roh, S. U. Z. Khan, B. P. Rand, *Adv. Mater.* **2019**, *31*, 1805836.

[5] a) Y. Cao, N. Wang, H. Tian, J. Guo, Y. Wei, H. Chen, Y. Miao, W. Zou, K. Pan, Y. He, *Nature* **2018**, *562*, 249; b) K. Lin, J. Xing, L. N. Quan, F. P. G. de Arquer, X. Gong, J. Lu, L. Xie, W. Zhao, D. Zhang, C. Yan, *Nature* **2018**, *562*, 245; c) M. Ban, Y. Zou, J. P. Rivett, Y. Yang, T. H. Thomas, Y. Tan, T. Song, X. Gao, D. Credington, F. Deschler, *Nat. Commun.* **2018**, *9*, 3892; d) Z. Chen, C. Zhang, X. F. Jiang, M. Liu, R. Xia, T. Shi, D. Chen, Q. Xue, Y. J. Zhao, S. Su, *Adv. Mater.* **2017**, *29*, 1603157; e) B. Zhao, S. Bai, V. Kim, R. Lamboll, R. Shivanna, F. Auras, J. M. Richter, L. Yang, L. Dai, M. Alsari, *Nat. Photonics* **2018**, *12*, 783.

[6] a) Z. Li, T. R. Klein, D. H. Kim, M. Yang, J. J. Berry, M. F. van Hest, K. Zhu, *Nat. Rev. Mater.* **2018**, *3*, 18017; b) M. Shibata, Y. Sakai, D. Yokoyama, *J. Mater. Chem. C* **2015**, *3*, 11178.

[7] a) C. W. Tang, S. A. VanSlyke, *Appl. Phys. Lett.* **1987**, *51*, 913; b) H. Yamamoto, J. Wilkinson, J. P. Long, K. Bussman, J. A. Christodoulides, Z. H. Kafafi, *Nano Lett.* **2005**, *5*, 2485; c) R. Zhang, H. Zheng, J. Shen, *Synth. Met.* **1999**, *106*, 157.

[8] K. L. Gardner, J. G. Tait, T. Merckx, W. Qiu, U. W. Paetzold, L. Kootstra, M. Jaysankar, R. Gehlhaar, D. Cheyns, P. Heremans, *Adv. Energy Mater.* **2016**, *6*, 1600386.

[9] a) C. W. Chen, H. W. Kang, S. Y. Hsiao, P. F. Yang, K. M. Chiang, H. W. Lin, *Adv. Mater.* **2014**, *26*, 6647; b) C. Y. Chen, H. Y. Lin, K. M. Chiang, W. L. Tsai, Y. C. Huang, C. S. Tsao, H. W. Lin, *Adv. Mater.* **2017**, *29*, 1605290; c) M. Kam, Y. Zhu, D. Zhang, L. Gu, J. Chen, Z. Fan, *Sol. RRL* **2019**, *3*, 1900050.

[10] a) K.-M. Chiang, B.-W. Hsu, Y.-A. Chang, L. Yang, W.-L. Tsai, H.-W. Lin, *ACS Appl. Mater. Interfaces* **2017**, *9*, 40516; b) Y. Hu, Q. Wang, Y.-L. Shi, M. Li, L. Zhang, Z.-K. Wang, L.-S. Liao, *J. Mater. Chem. C* **2017**, *5*, 8144.

[11] J. Li, P. Du, S. Li, J. Liu, M. Zhu, Z. Tan, M. Hu, J. Luo, D. Guo, L. Ma, *Adv. Funct. Mater.* **2019**, *29*, 1903607.

[12] a) N. Yantara, S. Bhaumik, F. Yan, D. Sabba, H. A. Dewi, N. Mathews, P. P. Boix, H. V. Demir, S. Mhaisalkar, *J. Phys. Chem. Lett.* **2015**, *6*, 4360; b) D. Zhang, L. Gu, Q. Zhang, Y. Lin, D.-H. Lien, M. Kam, S. Poddar, E. C. Garnett, A. Javey, Z. Fan, *Nano Lett.* **2019**, *19*, 2850.

[13] a) J. Byun, H. Cho, C. Wolf, M. Jang, A. Sadhanala, R. H. Friend, H. Yang, T. W. Lee, *Adv. Mater.* **2016**, *28*, 7515; b) Z. Li, Z. Chen, Y. Yang, Q. Xue, H.-L. Yip, Y. Cao, *Nat. Commun.* **2019**, *10*, 1027; c) L. N. Quan, Y. Zhao, F. P. García de Arquer, R. Sabatini, G. Walters, O. Voznyy, R. Comin, Y. Li, J. Z. Fan, H. Tan, *Nano Lett.*

[14] a) M. Yuan, L. N. Quan, R. Comin, G. Walters, R. Sabatini, O. Voznyy, S. Hoogland, Y. Zhao, E. M. Beauregard, P. Kanjanaboos, *Nat. Nanotechnol.* **2016**, *11*, 872; b) H. Hu, T. Salim, B. Chen, Y. M. Lam, *Sci. Rep.* **2016**, *6*, 33546; c) Y. H. Kim, H. Cho, J. H. Heo, T. S. Kim, N. Myoung, C. L. Lee, S. H. Im, T. W. Lee, *Adv. Mater.* **2015**, *27*, 1248; d) N. Wang, L. Cheng, R. Ge, S. Zhang, Y. Miao, W. Zou, C. Yi, Y. Sun, Y. Cao, R. Yang, *Nat. Photonics* **2016**, *10*, 699.

[15] a) Y. Chen, Y. Sun, J. Peng, J. Tang, K. Zheng, Z. Liang, *Adv. Mater.* **2018**, *30*, 1703487; b) P. Chen, Y. Bai, M. Lyu, J. H. Yun, M. Hao, L. Wang, *Sol. RRL* **2018**, *2*, 1700186; c) T. M. Koh, V. Shanmugam, J. Schlipf, L. Oesinghaus, P. Müller-Buschbaum, N. Ramakrishnan, V. Swamy, N. Mathews, P. P. Boix, S. G. Mhaisalkar, *Adv. Mater.* **2016**, *28*, 3653; d) M. I. Saidaminov, O. F. Mohammed, O. M. Bakr, *ACS Energy Lett.* **2017**, *2*, 889.

[16] Y. Tan, R. Li, H. Xu, Y. Qin, T. Song, B. Sun, *Adv. Funct. Mater.* **2019**, *29*, 1900730.

[17] J. Ávila, C. Momblona, P. P. Boix, M. Sessolo, H. J. Bolink, *Joule* **2017**, *1*, 431.

[18] a) G. Jia, Z.-J. Shi, Y.-D. Xia, Q. Wei, Y.-H. Chen, G.-C. Xing, W. Huang, *Opt. Express* **2018**, *26*, A66; b) P. Chen, Y. Meng, M. Ahmadi, Q. Peng, C. Gao, L. Xu, M. Shao, Z. Xiong, B. Hu, *Nano Energy* **2018**, *50*, 615; c) H. Zheng, G. Liu, L. Zhu, J. Ye, X. Zhang, A. Alsaedi, T. Hayat, X. Pan, S. Dai, *Adv. Energy Mater.* **2018**, *8*, 1800051.

[19] A. Vailionis, H. Boschker, Z. Liao, J. Smit, G. Rijnders, M. Huijben, G. Koster, *Appl. Phys. Lett.* **2014**, *105*, 131906.

[20] L. A. Frolova, D. V. Anokhin, A. A. Piryazev, S. Y. Luchkin, N. N. Dremova, K. J. Stevenson, P. A. Troshin, *J. Phys. Chem. Lett.* **2017**, *8*, 67.

[21] a) R. Yang, R. Li, Y. Cao, Y. Wei, Y. Miao, W. L. Tan, X. Jiao, H. Chen, L. Zhang, Q. Chen, *Adv. Mater.* **2018**, *30*, 1804771; b) J. Xing, Y. Zhao, M. Askerka, L. N. Quan, X. Gong, W. Zhao, J. Zhao, H. Tan, G. Long, L. Gao, *Nat. Commun.* **2018**, *9*, 3541.

[22] a) S. Silver, J. Yin, H. Li, J. L. Brédas, A. Kahn, *Adv. Energy Mater.* **2018**, *8*, 1703468; b) Z. Wang, Q. Lin, F. P. Chmiel, N. Sakai, L. M. Herz, H. J. Snaith, *Nat. Energy* **2017**, *2*, 17135; c) N. Zhou, Y. Shen, L. Li, S. Tan, N. Liu, G. Zheng, Q. Chen, H. Zhou, *J. Am. Chem. Soc.* **2018**, *140*, 459.

[23] N. Cho, F. Li, B. Turedi, L. Sinatra, S. P. Sarmah, M. R. Parida, M. I. Saidaminov, B. Murali, V. M. Burlakov, A. Goriely, *Nat. Commun.* **2016**, *7*, 13407.

[24] L. Nie, X. Ke, M. Sui, *Nanomaterials* **2019**, *9*, 722.